Flow and reaction along the interface between hydrated Portland cement and calcareous rocks during CO$_2$ injection. Laboratory experiments and modeling.

Lídia Fernández-Rojo[1,2], Josep M. Soler[1], M. Gabriela Dávila[3], M. Carme Chaparro[4], Ignasi Queralt[1], Jordi Cama[1*]

[1] Institute of Environmental Assessment and Water Research (IDAEA), CSIC. Jordi Girona 18-26, Barcelona 08034, Catalonia, Spain.

[2] Centre Tecnològic Eurecat. Plaça de la Ciència 2, Manresa 08242, Catalonia, Spain.

[3] Purdue University (PU), Department of Earth, Atmospheric, and Planetary Sciences. West Lafayette, IN, 47907, USA.

[4] Karlsruhe Institute of Technology (KIT), Institute of Nuclear Waste Disposal (INE). PO BOX 3640, 76021, Karlsruhe, Germany.

*Corresponding author (jordi.cama@idaea.csic.es)

20

Abstract

To better understand the geochemical alteration of the interface between wellbore Portland cement and rock because of potential leakage during CO_2 storage operations, we performed percolation experiments using three solid cores each made of two half-cylinders, one of hydrated Portland cement and the other of calcareous rock (limestone, marl or sandstone). These experiments were run under atmospheric ($P_{CO2}= 10^{-3.4}$ bar and room temperature) and supercritical ($P_{CO2} = 130$ bar and 60 ºC) CO_2 conditions with an injection pH of 6.4 and 3.2, respectively. The variation in the aqueous chemistry of the outflows was reproduced by 2D reactive transport simulations.

The experimental and model results showed that under atmospheric conditions, a slight dissolution of portlandite and C-S-H near the cement-channel interface was responsible for an incipient alteration of cement that was prevented by the precipitation of brucite. By contrast, under supercritical conditions, cement alteration was marked owing to an intense dissolution of cementitious phases (portlandite, ettringite, Si-hydrogarnet and hydrotalcite), causing an increase in porosity.

Overall, the results show that potential CO_2 leakage during and after CO_2 injection will cause an alteration of the hydrated Portland cement, resulting in a loss of its sealing properties. The alteration of low-porosity calcareous rocks, such as the ones used in this study, is only expected to be minor.

Keywords

CO_2 storage, Portland cement, limestone, marl, sandstone, reactivity

42

44

1 Introduction

46   One of the major risks involved during geological CO_2 storage is the possibility of

47   CO_2 leakage along injection, monitoring and legacy wells (Gasda et al., 2004; Benson

48   and Cole, 2008). Along a wellbore, CO_2 leakage can occur through cracks,

49   microfractures, flow channels in cementation, along the cement-rock spaces, and

50   through microannuli generated during CO_2 injection (Celia and Bachu, 2003; Barlet-

51   Gouédard et al., 2009; Scherer and Huet, 2009; Watson et al., 2009; Carey et al., 2010;

52   Zhang and Bachu, 2011; Harvey et al., 2013; Abid et al., 2015; Zhang et al., 2015;

53   Bagheri et al., 2018; Onishi et al., 2019).

54   For a quantitative spatiotemporal evolution of potential CO_2 leakage pathways

55   along wellbore cementation and surrounding rocks as CO_2-saturated brines pass

56   through, percolation experiments with artificially fractured cement cores (Wigand et al.,

57   2009; Abdoulghafour et al., 2013, 2016; Huerta et al., 2013, 2016; Luquot et al., 2013;

58   Cao et al., 2015) and fractured rock-cement cores (Mason et al., 2013; Newell and

59   Carey, 2013; Walsh et al., 2014; Connell et al., 2015; Brunet et al., 2016; Carroll et al.,

60   2017) have been carried out under wellbore conditions.

61   In some of these studies, multicomponent reactive transport (MRT) modeling was

62   used for a quantitative understanding of the geochemical alteration of cement-rock

63   fractures reacting with flowing CO_2-saturated water in order to predict the long-term

64   degradation of wellbore cement and well integrity (Cao et al., 2015; Connell et al.,

65   2015; Abdoulghafour et al., 2016; Brunet et al., 2016; Carroll et al., 2017). Parameters

66   such as fracture/channel length, injection rate, residence time and brine composition

67   have been shown to influence the evolution of fracture permeability (e.g., Brunet et al.,

2016). Other studies have made use of batch experiments (static flow conditions) with non-fractured rock-cement cores (Duguid et al., 2011; Sterpenich et al., 2104 and Nakano et al., 2017). Their findings not only highlight the importance of the residence time and brine composition to regulate the mineralogical evolution of the rock-cement interface but also the major role of the dissolution and precipitation rates and the rates of diffusion of the reacting species on cement carbonation.

In these earlier works, the rocks selected to study the alteration in cement-rock fractures by CO_2-saturated fluids have been mainly quartz sandstones. In the percolation experiments presented here, three calcareous rocks, limestone, argillaceous limestone (referred to here as marl) and clast-poor cement-rich quartz sandstone, with high calcite contents (99, 86 and 68 wt.%, respectively; Garcia-Rios et al., 2017; Dávila et al., 2016a) were used to study the alteration of the cement-rock system under supercritical CO_2 pressure ($P_{TOT} = P_{CO2} = 130$ bar and 60 °C) and under normal atmospheric conditions ($P_{TOT} = 1$ bar, $P_{CO2} = 10^{-3.4}$ bar and 22 °C). A novel aspect of this study is that during the experiments, synthetic groundwater circulated along a flow channel between cement and rock. Length and aperture of the channel were 4.7 - 4.9 cm and 300 - 500 μm, respectively. Since water was injected at a constant flow rate of 0.06 mL/min, mean water residence times were short, ranging between 1.9 and 4.7 min (Table 1). The initial diffusivity of the hydrated Portland cement was determined by means of short pulse tracer tests.

Moreover, in our study the injected fluid was a synthetic groundwater with a chemical composition similar to that of the sulfate-rich groundwater at the Hontomín site (Spain; Garcia-Rios et al., 2015). 2D reactive transport simulations using CrunchFlow (Steefel et al., 2015) were used to quantitatively interpret the experimental results in terms of rock and cement reactivities and transport properties.

93

2 Materials and methods

95

2.1 Experimental design

97 Two experimental setups were used to carry out the experiments under supercritical

98 (*supc*; P_{CO2} = 130 bar, T = 60ºC) and atmospheric (*atm*; P_{CO2} = $10^{-3.4}$ bar, T = 25ºC)

99 CO_2 conditions (Fig. 1). Three flow-through experiments with three different cores were

100 performed for each experimental setup. The experimental conditions are summarized in

101 Table 1. The cores were made of two half-cylinders, one of hydrated Portland cement

102 and the other one of calcareous rock (limestone, marl or sandstone). 1885 g of Portland

103 cement (sulfate-resistant CEM I 42.5R/SR were mixed with 717 g of deionized water

104 (standard water-to-cement ratio for Class H cement; w/c = 0.38; Pang (2015)). The

105 hydrated cement was cured in a moisture room to ensure that hydration continued for 91

106 days in order to reach maximum strength, durability and sufficient impermeability.

107 Cement consisted of C-S-H (Calcium Silicate Hydrate, 46.6 wt.% with a Ca/Si ratio of

108 1.67), portlandite (24.6 wt.%), and smaller amounts of ettringite, calcite, hydrotalcite

109 and Si-hydrogarnet (13.1, 4.1, 3.3 and 8.3 wt.%, respectively). The rock samples

110 consisted mainly of calcite with variable quantities of other mineral phases. The

111 limestone sample contained calcite and quartz, (99 and 1 wt.%, respectively), the

112 sandstone sample contained calcite, quartz, illite and microcline (67.6, 24.4, 4.6 and 3.3

113 wt.%, respectively) and the marl sample was made up of calcite, quartz, illite, albite,

114 chlinochlore, gypsum and pyrite (71.2, 9.9, 6.9, 6.8, 2.8, 2.2, and ~ 0.2 wt%,

115 respectively).

116 In the supercritical experiments, thin planar channels of 0.3-0.5 mm aperture, 12-13 mm

117 width and 47-49 mm length were cut into the rock half-cylinder with a drill/grinder

118 precision tool (Parkside PFBS 12 B2). In the atmospheric experiments, two narrow

119 PVC films of 0.5-mm thickness, 7.5-mm width and 24-mm length were placed between

120 the rock and the cement half-cylinders and at a distance of 10 mm from each other, thus

121 creating a single straight channel (Fig. 2). Filters of 4.5-µm pore size were placed at the

122 inlet and outlet of each core.

123 The saline solution used in the experiments was a synthetic version of the Hontomín

124 groundwater (Garcia-Rios et al., 2015). It was prepared in the laboratory by adding

125 appropriate amounts of NaCl, $CaCl_2 \cdot 2H_2O$, $MgCl_2 \cdot 6H_2O$, KCl, Na_2SO_4 and NaBr in

126 double deionized water (DDW, Merck Millipore Milli-Q®). The saline solution

127 contained on average (mol/kgw) 4.91×10^{-2} Ca, 3.24×10^{-2} Mg, 1.13×10^{-2} K, $3.89 \times$

128 10^{-1} Na, 2.68×10^{-2} S(SO$_4$), 4.98×10^{-1} Cl and 1.14×10^{-2} Br and was in equilibrium

129 with gypsum. The pH of the injected solution after equilibration with CO_2 varied

130 between 6.2 and 6.4 in the atmospheric experiments and between 3.1 and 3.3 in the

131 supercritical experiments (Table 2).

132 The supercritical CO_2 reactor was made of type-316 stainless steel, resistant to acid

133 solutions. The whole circuit was connected using stainless Swagelok tubing of 1.08-

134 2.29-mm inner diameter. The setup consisted of two water tanks each with one-liter

135 capacity, a compressor (Maximator, DLE 5-30-GG-C), a custom-made double piston

136 pump, a sample holder, and a double syringe sampling system. The compressor

137 increased the CO_2 gas pressure up to 130 bar in the two one-liter saline solution tanks.

138 The pump supplied the CO_2-equilibrated saline solution to the inlet of the cement-rock

139 core inside the sample holder at a constant flow rate of 0.06 mL/min. Before being

140 placed inside the holder, the cores were wrapped with inner multilayers of Teflon and

7

141 an outer layer of cold shrink silicone rubber to isolate them from confining water. A

142 pressure multiplier increased the confining pressure in the sample holder to 150 % of

143 the inlet pressure in order to mimic the natural confining conditions. The output solution

144 was collected in a pressurized double syringe equipped with a back-pressure system that

145 maintained the pressure at 130 bar. The temperature of the circuit was maintained at 60

146 ºC by means of heaters that covered each water tank and the sample holder. The

147 experiments lasted 350 h (limestone) and 500 h (sandstone and marl).

148 The atmospheric CO_2 reactor consisted of a solution tank connected to a peristaltic

149 pump (Gilson, Minipuls 3) that continuously supplied the solution to the inlet of the

150 core at a constant flow rate of 0.05 mL/min. The reacted solution was collected for

151 further analyses. The room temperature was set to 22 ± 3 ºC. A tracer test with 1 g/L

152 LiBr was performed at the start of the atmospheric experiments (5 h) to determine the

153 initial effective diffusion coefficient of the hydrated Portland cement. The experiments

154 lasted for 1750 h.

155

156

157 **2.2 Chemical and mineralogical analyses**

158 Output solutions were filtered (Frisenette, pore size 0.22 μm) and immediately acidified

159 and diluted (dilution of 1/200) to a final concentration of 1% HNO_3. Total

160 concentrations of Ca, Mg, K, Na, S, Fe, Si, Al and Li were determined by Inductively

161 Coupled Plasma-Optical Emission Spectroscopy (ICP-OES) with different instruments

162 (Perkin Elmer Optima 8300, Perkin Elmer Optima 3200RL, and Thermo Scientific

163 iCAP 6500 Radial). Analytical detection limits for Ca, S, Mg, Si, Na, Al, K, Fe and Li

164 were 1.3×10^{-6}, 6.2×10^{-6}, 2.1×10^{-6}, 1.8×10^{-6}, 1.3×10^{-4}, 1.9×10^{-6}, 1.3×10^{-5}, $7.1 \times$

165 10^{-7} and 9.6×10^{-7} mol/L, respectively. Owing to the dilution factor, detection limits in

166 output samples were 200 times higher. The uncertainty in measured elements was better

167 than $\pm$ 3%. Note, however, that small differences between the high concentrations of the

168 input and output solutions led to propagated errors of about 6%. Concentrations of Cl

169 and Br were anticipated to be conservative and were not measured.

170 Initial rock compositions were obtained by X-ray diffraction (Bruker D8 A25 Advance

171 X-ray diffractometer θ-θ, with CuKα1 radiation) combined with Rietveld analysis. Rock

172 porosities were taken from Dávila et al. (2016a) and García-Rios et al. (2017). To

173 identify the mineralogical changes, the samples were analyzed after the experiments

174 with Scanning Electron Microscopy (SEM) employing a JEOL JSM-840 instrument

175 under a 15–20 kV using the backscattered electron detector (BSE)) and thereafter with

176 XRD. The initial and final channel apertures in the *supc*-CO$_2$ experiments were

177 determined by confocal microscopy (Leica DCM3D) in limestone and sandstone

178 samples. This technique was also employed to analyze one altered cement face. The

179 initial aperture in the marl core was determined with a surface profilometer (Veeco

180 Dektak 150).

181

182 **2.3   Reactive transport modeling**

183 The experimental results (evolution of solution chemistry at the outlet and changes in

184 mineralogy) were interpreted by means of reactive transport modeling using

185 CrunchFlow (Steefel et al., 2015) and following an approach similar to that used by

186 Dávila et al. (2016a) and García-Ríos et al. (2017). Figure 2 shows the type of two-

187 dimensional (2D) numerical domain that was used in the simulations. The domain

188 includes the rock and cement zones, separated by the synthetic flow channel. Water

189 flow only takes place in the channel. Solute transport in both rock and cement zones

190   occurs only by diffusion. The fitting of the model to the experimental results was

191   performed by adjusting the values of the reactive surface areas in the reaction rate laws

192   (mineral and cement-phase reactivities), using the reaction rate laws from the literature.

193   When required, the initial diffusion coefficients were also adjusted in the cement or rock

194   zones. The match between the experimental and model results was deemed valid when

195   both the aqueous chemistry of the output solutions (within error) and the mineral

196   composition of the solid (i.e., presence and proportions of the minerals) were

197   simultaneously reproduced.

198   The three-dimensional experimental setup was transformed into a 2D problem as shown

199   in Fig. 2. The channel aperture and cross section were maintained. The cylindrical

200   section of the column setup was converted into a rectangular section by conserving the

201   area and width (diameter) of the cylindrical sections and by calculating the thickness of

202   each rectangular subsection (rock and cement). The numerical domain would then

203   correspond to a 2D section of the resulting rectangular prism that is parallel to the flow

204   direction and perpendicular to the channel plane. No-flux conditions were applied to all

205   external boundaries of the domain, except where water flows into or out of the channel.

206   Advective flux conditions (concentration times flow velocity) were used at those points.

207   Table S1 in Supplementary Information (SI) shows the details of the numerical spatial

208   discretizations that were implemented.

209   Table 3 displays the initial composition of rock and cement (vol.% of minerals and

210   cement phases) in the different experiments. The corresponding porosities are given in

211   Table 4. Porosity, solid-phase and porewater compositions of the hydrated cement were

212   obtained from a thermodynamic calculation of the hydration process performed at

213   EMPA (Switzerland) using the GEMS code (Kulik et al., 2013; gems.web.psi.ch) and

214   following the procedure described by Lothenbach and Winnefeld (2006) and

215   Lothenbach and Wieland (2006).

216   Table 2 shows the composition of the input solutions in the different experiments

217   together with the initial solution compositions in each of the domains (rock and

218   cement). The initial composition of the water in the channel was set to be the same as

219   that of the input solution. Note that with the short water residence times in the

220   experiments (Table 1), the choice of the initial channel water composition had little

221   effect. Initial rock solutions are in equilibrium with calcite and quartz, while initial

222   cement solutions are in equilibrium with the primary cement phases (Table S2 in SI).

223   Secondary phases in the rock domain were all initially undersaturated except for

224   gypsum (practically in equilibrium). Secondary phases in the cement zone were also

225   undersaturated except for brucite (supersaturated under atmospheric conditions) and

226   ferrihydrite (slightly supersaturated under supercritical conditions). Speciation in

227   solution (Table S4 in SI) was calculated using the EQ3/6 database included in the code

228   (Wolery et al., 1990). Initially dissolved CO_2 in the input solution for the experiments

229   under supercritical conditions was calculated employing the model by Duan and Sun

230   (2003). Table S5 in SI shows the equilibrium constants for the different solid phases

231   that were used in the calculations. Note that calculations were performed at 25 °C

232   although the atmospheric pressure experiments were carried out at room temperature

233   (22 ± 3 °C).

234   In CrunchFlow, solid-phase dissolution and precipitation reactions are always

235   implemented through kinetic reaction rate laws (see Eqs. (S1) and (S2) in SI). The rate

236   laws used in the calculations are expressed as a function of the bulk surface area (A_m in

237   m^2/m^3), the reaction rate constant at the temperature of interest ($k_{m.T}$ in mol/m^2/s), a term

238   that describes the dependence of the rate on pH (a_{H+}^n) in which a_{H+} is the activity of H$^+$,

239   and the dependence on the saturation state. The procedure to adjust mineral surface

240   areas started by assigning large areas (10^5 to 10^6 m^2/m^3) to all minerals in all the zones

241   (rock, cement, channel), corresponding to local equilibrium conditions for mineral

242   reaction. Next, surface areas were reduced for different phases in the different zones in

243   order to match the experimental results. Table 3 shows the adjusted values of the

244   surface areas in addition to the initial volumetric contents. The shaded values in the

245   table indicate the values that were reduced in order to obtain a good match between the

246   model and the experimental results.

247   As regards solute transport, advection and dispersion only take place along the channel.

248   Darcy velocity (volumetric water flux in $m^3/m^2/s$) is constant during each experiment.

249   Transport is only by diffusion in the cement and rock zones. Effective diffusion

250   coefficients (m^2/s) are calculated according to

251                   $D_e = \phi \tau D_0$ (1)

252   where ϕ is porosity, τ is tortuosity and D_0 is a reference diffusion coefficient (constant).

253   Initial D_e values are given by the value of D_0, which is a constant for the whole model,

254   the initial porosity, which is characteristic of each zone, and a value of tortuosity, which

255   is also representative of each zone and constant throughout the calculation. With this

256   formulation, D_e changes linearly with porosity as porosity changes owing to dissolution

257   and precipitation. Table 4 lists Darcy velocities and dispersivities in the channel for

258   each experiment together with the initial D_e and ϕ values for the different zones. With

259   these parameters it is possible to calculate the characteristic times for advection (mean

260   water residence time along the flow channel) and diffusion (t_{dif}, mean time for a particle

261   to diffuse across the cement or rock domain to the flow channel) according to

262                   $t_{dif} = thickness^2/(2D_e/\phi)$ (2)

263   where *thickness* refers to the thickness (normal to the flow direction) of the cement or

264   rock model domain. The characteristic times for advection were in the 100 to 300 s

265   range (Table 2), whereas the characteristic times for diffusion were in the 10^5 s (cement)

266   and 10^5 to 10^6 s (rock) ranges. The composition of the flowing water is strongly

267   dominated by advection; the large advective solute fluxes in the channel prevent any big

268   changes in solution composition resulting from diffusion and reaction with cement or

269   rock.

270   ## 3   Results and discussion

271

272   ### 3.1   Initial tracer tests

273   A LiBr (1 g/L) tracer test (injection of a short tracer pulse) was performed for each of

274   the atmospheric experiments (25 °C) prior to the injection of the synthetic groundwater.

275   This initial tracer injection was included as an initial stage in the modeling of the

276   experiment, which was followed immediately by the injection of the synthetic

277   groundwater. In this first stage, the effective diffusion coefficient for the cement was

278   adjusted in order to match the model results with the measured tracer breakthrough

279   curve (Fig. 3). Given the similar rock porosity in all samples, the effective diffusion

280   coefficient was adjusted using data from the sandstone (*atm*-SC) experiment, which

281   showed a lower dispersion. Porosity and D_e values for the rock were based on those

282   reported by Dávila et al. (2016a) and García-Ríos et al. (2017). These D_e values are in

283   the 10^{-13} m^2/s range for the experiments with comparable flow rates and water residence

284   times. Since ϕ and D_e values in the cement are much higher than those in the rock, the

285   breakthrough curve is basically only sensitive to the D_e value in the cement. The D_e

13

286   values for cement obtained in these tracer tests range between 2.8×10^{-11} and 5.6×10^{-11}

287   m^2/s.

288

289   **3.2   Atmospheric CO_2 experiments**

290   Figure 4 shows the changes in solution composition between the input and output

291   solutions for the different experiments. Only pH and the concentrations of the elements

292   showing the largest changes are shown (Ca, S, Mg). Na and K results are included in

293   Fig. S1 in SI. Fe, Al and Si were below detection limit in these experiments.

294   In the atmospheric experiments, pH increased rapidly from the input value to about 11

295   during the initial tracer test (injection of a very dilute solution) because of the alkalinity

296   (OH^-) provided by the cement. However, pH dropped rapidly once the injection of the

297   synthetic groundwater commenced. The increase in pH was smaller during groundwater

298   injection (values between 8 and 9) than during the initial tracer test due to the

299   precipitation of brucite in the cement adjacent to the channel, which consumed OH^-. An

300   additional fall in pH could be observed later in the experiments (especially evident in

301   the limestone experiment; Fig. 4). This further change in pH was controlled by the

302   decrease in porosity in the cement close to the channel, which limits the diffusive solute

303   transport from cement to channel.

304   As for variations in the major-element composition of the solution, Fig. 4 shows that

305   Ca, Mg and S concentrations did not change significantly (all within the analytical

306   uncertainty range). However, the experimental observations revealed precipitation of

307   brucite and aragonite on the cement side of the channel (Fig. 5a,b and Fig. S2 in SI) and

308   minor calcite dissolution on the rock side of the channel (Fig. 5c,d and Fig. S2 in SI).

309   Notice that the high concentrations of these elements in the input solutions (Table 2)

14

310   and the short residence times of water in the channel (Table 1) prevented any large

311   changes in solution composition at the outlet (balance between the elemental fluxes at

312   the inlet and the consumption by diffusion into cement/rock and precipitation). This is

313   especially evident in the case of Mg, where no significant Mg deficit could be observed.

314   Given the dimensions of the channels in the three cores, channel permeability was too

315   high to be measured since the pressure difference ($\Delta P(t)$) between the inlet and the

316   outlet of the samples was negligible during the experiments. Although morphological

317   changes were visible along the channels (Fig. 7), permeability remained high

318   throughout the experiments.

319   The model results show significant brucite precipitation in the cement adjacent to the

320   channel (Fig. 8 and Fig. S3 in SI) together with some gypsum precipitation and strong

321   portlandite dissolution (source of Ca and OH$^-$). The resulting alteration zone extends for

322   about 1 mm into the cement. Diffusion of the Mg in the input solution together with the

323   alkalinity in the cement induces the precipitation of brucite. Gypsum precipitation is

324   induced by Ca from portlandite dissolution and sulfate from the input solution. The

325   precipitation of brucite is the main process responsible for the decrease in porosity in

326   the cement close to the channel (Fig. 9 and Figs. S4 and S5 in SI). Calcite precipitation

327   was not allowed in the calculations in order to facilitate precipitation of aragonite in the

328   cement domain; sporadic aragonite precipitation was detected in the SEM images (Fig.

329   5b). Model results only show very minor calcite dissolution on the rock side of the

330   channel.

331

332   **3.3   Supercritical CO$_2$ experiments**

333   The input solution during the supercritical experiments was acidic (pH about 3) owing

334   to the equilibration with CO$_2$ at 130 bar. This acidic solution was further from

15

335   equilibrium with the cement phases than the corresponding solution in the atmospheric

336   experiments. As a result, the magnitude of the reactions was markedly greater, giving

337   rise to more significant changes in solution chemistry (Fig. 4). pH increased from about

338   3 to 4, which corresponds to a much larger consumption of H^+ compared with the

339   atmospheric experiments.

340   In these experiments, the measured changes in solution are still relatively small (within

341   the analytical error for many of the measurements; Fig. 4). However, the changes

342   indicate clear trend towards an increase in Ca concentration and decrease in S

343   concentration (portlandite dissolution and sulfate precipitation). By contrast, changes in

344   Mg concentration are smaller (more clearly within analytical error).

345   Although the results of the model reproduced qualitatively the increase in Ca

346   concentration, there is no significant change in Mg and S concentrations. As for the

347   solid phases, the results of the model show intense dissolution of portlandite, ettringite,

348   Si-hydrogarnet and hydrotalcite, extending for about 3 mm into the cement, thereby

349   leading to an increase in porosity (Fig. 8 and Fig. S3 in SI). As portlandite, ettringite

350   and Si- hydrogarnet dissolve, the Ca released is precipitated mainly as calcite, with

351   carbonate being provided by the input solution. A dissolution front is created, and as it

352   moves into the cement, calcite dissolves next to the channel (Fig. 6), where the acidic

353   solution is circulating. C-S-H only dissolves slightly near the channel-rock interface. A

354   gypsum precipitation front develops in the model at the portlandite-ettringite-

355   hydrogarnet dissolution front. This gypsum is replaced by calcite as the reaction front

356   advances towards the interior of the cement domain, leading to a small gypsum peak

357   right at the reaction front (Fig. 8). In the limestone case, the model also predicts an even

358   smaller gypsum peak at the calcite dissolution front next to the channel (Fig. 8). And

359   some very minor gypsum precipitation is also predicted in the rock in the marl case.

360   However, gypsum precipitation was not detected in these experiments (Fig. 6 and Fig.

361   S6 in SI). The high pressure (P_{TOT} = 130 bar) increases the equilibrium constant ($\log K$ =

362   -4.57) with respect to that at atmospheric pressure ($\log K$ = -4.74). The calculations also

363   resulted in the precipitation of small amounts of ferrihydrite, gibbsite and boehmite,

364   which could correspond to the Fe- and Al-rich precipitates observed in the channel (Fig.

365   8 and Fig. S3 in SI). The marked dissolution of portlandite, ettringite, Si-hydrogarnet

366   and hydrotalcite was responsible for the considerable loss of volume in the cement (Fig.

367   7), which induced an increase in porosity (Fig. 9 and Figs. S4 and S5 in SI).

368   On the rock side of the channel, preferential flow paths caused the formation of

369   channeled dissolution features in the limestone and marl (Fig. 7), whereas the

370   dissolution was uniform in the sandstone experiment (although some rugosity

371   developed due to the preferential dissolution of calcite over quartz). These features

372   could not be captured by the calculations owing to the 2D nature of the model, which

373   can only provide an average behavior across the width of the flow channel. Formation

374   of these dissolution patterns was previously observed in fractured cores of limestone

375   and sandstone under supercritical CO_2 conditions (Garcia-Rios et al., 2017).

376

377   **3.4   Effect of dissolved CO_2 on rock and cement reactivity**

378   As regards the reactivity of the primary cement phases, smaller surface areas were

379   implemented for ettringite, siliceous hydrogarnet and portlandite in the experiments

380   performed under atmospheric conditions (Table 3). By contrast, larger areas (inducing

381   fast reaction kinetics and local equilibrium conditions) were used for the experiments

382   under supercritical CO_2 conditions. This highlights the greater reactivity of cement

383   under geological storage conditions, in response to the higher P_{CO2} and T conditions and

384   their impact on solution composition. Reaction rate laws were used to account for the

17

385   reactivity of the cement phases ($R = k \cdot A \cdot \Omega$ (Eq. (S1) in SI) where k is the reaction rate

386   constant, A is the reactive surface area and Ω is the solution saturation state).

387   Calibration was performed by adjusting the reactive surface areas (A). However, these

388   changes in the A parameter values do not mean that the actual physical surface areas

389   were different in different experiments. What is adjusted is the net reactivity of the solid

390   phase.

391   For the minerals in the rock, the small diffusion coefficients implied a full solute

392   transport control of the reactions. Local equilibrium (provided by the large reactive

393   areas) was applied to both atmospheric and supercritical CO_2 pressures and

394   temperatures.

395   Under atmospheric conditions, the adjusted initial D_e value for the cement in the

396   experiment with sandstone (*atm*-SC, 2.8×10^{-11} m^2/s, Table 4) is consistent with the

397   value obtained in the LiBr tracer test. Similarly, under supercritical CO_2 conditions, the

398   values in all the experiments (6.5×10^{-11} m^2/s) are consistent with the increased

399   temperature of 60 °C and an activation energy for diffusion of about 19 to 21 kJ/mol

400   (Van Loon et al., 2005, and references within). The values for the limestone (atm-LC)

401   and marl (atm-MC) experiments under atmospheric conditions are higher (5.6×10^{-11}

402   m^2/s), but are nevertheless compatible with the results of the initial tracer tests (Fig. 3).

403   The adjusted initial reactive surface areas for portlandite (the most reactive cement

404   phase) in these experiments (atm-LC, 800 m^2/m^3; atm-MC, 100 m^2/m^3, Table 3) were

405   also larger than that for sandstone (atm-SC; 10 m^2/m^3). Since both the reactive surface

406   area and the diffusion coefficient control the overall reactivity, the two parameters are

407   probably correlated to some degree during the fitting procedure, with some of the

408   reactivity being assigned to an increased diffusion coefficient.

409

4   Summary and conclusions

The interface between rock and borehole cementation is a possible leakage pathway during deep geological injection of CO_2. Laboratory experiments involving flow along this interface were performed to study the alteration in hydrated Portland cement and rock. Experiments were carried out under (a) atmospheric conditions ($10^{-3.4}$ bar CO_2, 25ºC, pH 6.2) and (b) supercritical conditions (130 bar CO_2, 60ºC, pH about 3). Tracer (LiBr) tests were performed prior to the injection of the saline solution in the atmospheric experiments to characterize cement diffusivity. Because of the dimensions, rock and cement diffusivities and the rates of water flow, the system was dominated by advection. The evolution of solution chemistry at the outlet was monitored over time. Rock and cement were analyzed at the end of the experiments (SEM, XRD, confocal microscopy/profilometry).

In the atmospheric experiments, pH increased up to about 11 (tracer tests) and 8 (groundwater injection). Calculated outlet pH was about 4 under supercritical conditions. Major-element concentrations showed little change during the atmospheric experiments whereas some Ca excess and S deficit were observed under supercritical conditions. The small changes in solution chemistry were consistent with the short water residence times and reflected the dominant control of advection over diffusion in the rock and cement domains. Intense brucite precipitation was observed on the cement surface after the atmospheric experiments whereas an apparently amorphous red-colored phase precipitated under supercritical conditions. In the supercritical experiments, rock surfaces provided evidence of some calcite dissolution whereas in the atmospheric experiments alteration was smaller. Some gypsum precipitation was also observed. Interface aperture increased during the supercritical experiments.

435   The results of the 2D reactive transport model showed that, under atmospheric

436   conditions, brucite precipitation together with a decrease in porosity is brought about by

437   Mg diffusion in the input solution accompanied by the alkalinity in the cement. Ca

438   mainly from portlandite dissolution and sulfate from the input solution induce the

439   precipitation of gypsum. As for the supercritical experiments, which are characterized

440   by a highly dissolved CO_2 content and acidic pH (about 3), the results show intense

441   dissolution of portlandite, ettringite, siliceous hydrogarnet and hydrotalcite, extending

442   for about 3 mm into the cement, thereby causing an increase in porosity. The Ca

443   released precipitates as calcite with carbonate provided by the CO_2-rich input solution.

444   Some gypsum precipitation also takes place. Calcite dissolution and gypsum

445   precipitation also occur to a lesser degree on the rock side. These calculations also result

446   in the precipitation of small amounts of ferrihydrite, gibbsite and boehmite, which

447   probably correspond in part to the red-colored precipitates observed. Additional

448   amorphous phases may also be involved.

449   It should be noted that the behavior of the cement differs greatly in the two sets of

450   conditions. Under atmospheric conditions, brucite precipitation caused a sealing of

451   porosity in the cement, which prevented further alteration of the cement. However,

452   under supercritical conditions, alteration was much more pronounced. The input

453   solution was markedly more acidic with a highly dissolved CO_2 (carbonic acid) content.

454   This solution was further from equilibrium with the cement phases, and the lower pH

455   prevented the precipitation of brucite. The main secondary mineral in this case was

456   calcite (cement carbonation). Moreover, under supercritical conditions, the results of the

457   model indicate an increase in the reactivity of the cement. Model reactive surface areas

458   for portlandite, Si-hydrogarnet and ettringite were 2 to 4 orders of magnitude smaller

459   under atmospheric conditions.

460   To sum up, potential flow paths between borehole cementation (Portland cement) and

461   rock could bring about a considerable alteration in the cement because of the flow of

462   CO_2-rich solutions, increasing cement porosity and reducing its sealing properties. On

463   the other hand, the alteration of the calcareous rock is expected to be minor for the tight

464   rocks used in this study (small porosities, permeabilities and diffusivities: $\phi \approx$ 2-7 %, k

465    $< 10^{-18}$ m^2, $D_e \approx 10^{-13} - 10^{-12}$ m^2/s) compared with the high-porosity and high-

466   permeability rocks used in cement-rock core batch experiments (Salem and Lavoux

467   limestones and Berea sandstone, ϕ = 13-25% and $k \approx 10^{-13}$ m^2; Duguid et al., 2011;

468   Sterpenich et al., 2014; Nakano et al., 2017).

469

482   **Figure captions**

483   **Figure 1.** Experimental setup for a) supercritical and b) atmospheric CO_2 experiments.

484   **Figure 2.** Schemes showing a) the core sample, b) the geometrical transformation used

485   in the 2D modeling and c) the final 2D model domain with three defined geochemical

486   zones: zone 0 = channel, zone 1 = cement, zone 2 = rock.

487   **Figure 3.** Results from the tracer test performed at the start of the *atm*-SC experiment

488   and the corresponding adjusted models. D_e for the rock was fixed at $5.0 \times 10^{-13}\,\mathrm{m^2/s}$.

489   **Figure 4.** Experimental and model results for pH, dissolved Ca, S and Mg.

490   **Figure 5.** SEM images of the reacted samples after the experiments under atmospheric

491   pressure: a) cement showing brucite bed in the channel zone, with different

492   morphologies; b) limestone with sporadic aragonite crystals in the channel zone close to

493   the inlet; c) sandstone with pristine and channel zones close to the inlet and d) altered

494   marl with holes close to the inlet.

495   **Figure 6.** SEM images of the reacted samples after the experiments under CO_2

496   supercritical conditions: a) cement matrix and nodules composed of Al, Ca, Si, Fe

497   amorphous phases between inlet and outlet; b) limestone with dissolved calcite in the

498   channel zone close to the outlet; c) sandstone with dissolved calcite and unaltered

499   quartz grains in the channel zone close to the inlet and d) marl with a highly porous

500   channel zone close to the inlet.

501   **Figure 7.** 3D images of the core samples and measured lost volumes in supercritical

502   CO_2 experiments**.** The cement image corresponds to the supc-MC experiment. Lost

503   volumes in the channel zone (rock side or cement side) from simulations are included

504   for comparison. Note that amorphous phases coating the cement surface are not

505   satisfactorily reproduced.

506   **Figure 8.** Volumetric fractions of the main solid phases in a middle section profile

507   (1.25 cm and 2.30 cm from the inlet in *atm-CO$_2$* and *supc-CO$_2$*, respectively) at the end

508   of the experiments. Distance in the x axis is normalized to the core diameter (25 mm,

509   except 40.5 mm for *atm*-SC).

510   **Figure 9.** Initial and final calculated porosities in middle section profiles (1.25 cm and

511   2.30 cm from the inlet in *atm*-CO$_2$ and *supc*-CO$_2$, respectively). Distance in the x axis is

512   normalized to the core diameter (25 mm, except 40.5 mm for *atm*-SC).

513   **Table heads**

514

515   **Table 1** Experimental conditions.

516   **Table 2.** Chemical composition (ion concentration in mol/kgw), ionic strength (I), pH

517   of the injected and porewater solutions used in the simulations. For atm-CO$_2$

518   experiments it corresponds to the injected and porewater solutions after the tracer tests

519   phase. See Table S3 in SI for the chemical composition of the solutions used in the

520   simulations of the tracer tests.

521   **Table 3.** Adjusted mineral bulk surface areas (BSA) and volumetric fractions (Vol. F

522   %) of primary minerals used in the simulations.

523   **Table 4.** Transport parameters used in the simulations.

524   **References**

525

526   Abdoulghafour, H., Luquot, L., Gouze, P., 2013. Characterization of the

527   mechanismscontrolling the permeability changes of fractured cements flowed through

528   by CO$_2$-rich brine. Environ. Sci. Technol. 47, 10332–10338.

529   Abdoulghafour, H., Gouze, P., Luquot, L., Leprovost, R., 2016. Characterization and

530   modeling of the alteration of fractured class-G Portland cement during flow of CO_2-rich

531   brine. Int. J. Greenh. Gas Cont. 48, 155–170.

532   Abid, K., Gholami, R., Choate, P., Nagaratnam, B.H., 2015. A review on cement

533   degradation under CO2-rich environment of sequestration projects. J. NGSE, Elsevier

534   27, 1149-1157.

535   Bagheri, M., Shariatipour, S.M., Ganjian, E., 2018. A review of oil well cement

536   alteration in CO2-ricn environments. Const. Building Mat., 186, 946-948.

537   Benson, S.M., Cole, D.R., 2008. CO_2 sequestration in deep sedimentary formations.

538   Elements 4, 325–331.

539   Brunet, J.P., Li, L., Karpyn, Z. T., Huerta, N. J., 2016. Fracture opening or self-sealing:

540   Critical residence time as unifying parameter for cement-CO_2-brine interactions. Int. J.

541   Greenh. Gas Cont. 47, 25-37.

542   Carey, J.W., Svec, R., Grigg, R., Zhang, J., Crow, W., 2010. Experimental investigation

543   of wellbore integrity and CO2-brine flow along the casing-cement microannulus, Int. J.

544   Greenh. Gas Control. 4, 272–282.

545   Cao, P., Karpyn, Z.T., Li, L., 2015. Self-healing of cement fractures underdynamic flow

546   of CO_2-rich brine. Water Resour. Res. 51, 4684–4701.

547   Celia, M.A., Bachu, S., 2003. Geological sequestration of CO_2: Is leakage unavoidable

548   and acceptable?, in 6th International Conference on Greenhouse Gas Control

549   Technologies , edited by J. Gale and Y. Kaya, pp. 477–482, Pergamon, Oxford, U. K.,

550   doi:10.1016/B978-008044276-1/50076-3.

551   Connell, L., Down, D., Lu, M., Hay, D., Heryanto, D., 2015. An investigation into the

552   integrity of wellbore cement in CO_2 storage wells: Core flooding experiments and

553   simulations. Int. J. Greenh. Gas Cont. 37, 424–440.

554   Dávila, G., Luquot, L., Soler, J. M., Cama, J., 2016a. 2D reactive transport modeling of

555   the interaction between a marl and a CO_2-rich sulfate solution under supercritical CO_2

556   conditions. Int. J. Greenh. Gas Cont. 54, 145-159.

557   Dávila, G., Luquot L., Soler, J.M., Cama, J. 2016b. Interaction between a fractured marl

558   caprock and CO2-rich sulfatesolution under supercritical CO_2 conditions. Int. J. Greenh.

559   Gas Cont. 48, 105–119.

560   Duan, Z., Sun, R., 2003. An improved model calculating CO_2 solubility in pure water

561   and aqueous NaCl solutions from 273 to 533 K and from 0 to 2000 bar. Chem. Geol.

562   193, 257–271.

563   Duguid, A., Radonjic, M. and Scherer, G.W., 2011. Degradation of cement at the

564   reservoir/cement interface from exposure to carbonated brine. Int. J. Greenh. Gas Cont.

565   5, 1413-1428.

566   Gasda, S.E., Bachu, S., Celia, M.A., 2004. Spatial characterization of the location of

567   potentially leaky wells penetrating a deep saline aquifer in a mature sedimentary basin,

568   Environ. Geol. 46, 707–720.

569   García-Rios, M., Luquot, L., Soler, J.M., Cama, J., 2015. Influence of the flow rate on

570   dissolution and precipitation features during percolation of CO2-rich sulfate solutions

571   through fractured limestone samples. Chem. Geol. 414, 95-108.

572   García-Rios, M., Luquot, L., Soler, J. M., Cama, J., 2017. The role of mineral

573   heterogeneity on the hydrogeochemical response of two fractured reservoir rocks in

574   contact with dissolved CO_2. Appl. Geochem. 84, 202-217.

575   Harvey, O.R., Qafoku, N.P., Cantrell, K.J., Lee, G., Amonette, J.E., Brown, C.F., 2013.

576   Geochemical Implications of Gas Leakage associated with Geologic CO_2 Storage-A

577   Qualitative Review. Environ. Sci. Technol. 47, 23−36.

578   Huerta, N.J., Hesse, M.A., Bryant, S.L., Strazisar, B.R. Lopano, C.L., 2013.

579   Experimental evidence for self-limiting reactive flow through a fractured cement core:

580   Implications for time-dependent wellbore leakage. Environ. Sci. Technol. 47, 269−275.

581   Huerta, N.J., Hesse, M.A., Bryant, S.L., Strazisar, B.R., Lopano, C., 2016. Reactive

582   transport of CO_2-saturated water in a cement fracture: Application to wellbore leakage

583   during geologic CO_2 storage. Int. J. Greenh. Gas Cont. 44, 276–289.

584   Kulik, D. A., Wagner, T., Dmytrieva, S. V., Kosakowski, G., Hingerl, F. F.,

585   Chudnenko, K. V., Berner, U., 2013. GEM-Selektor geochemical modeling package:

586   revised algorithm and GEMS3K numerical kernel for coupled simulation codes.

587   Computational Geosciences 17, 1-24.

588   Lothenbach, B., Wieland, E., 2006. A thermodynamic approach to the hydration of

589   sulphate-resisting Portland cement. Waste Management 26, 706-719.

590   Lothenbach, B., Winnefeld, F., 2006. Thermodynamic modelling of the hydration of

591   Portland cement. Cement and Concrete Research 36, 209-226.

592   Luquot, L., Abdoulghafour, H., Gouze, P., 2013. Hydro-dynamically controlled

593   alteration of fractured Portland cements flowed by CO2-rich brine. International Journal

594   of Greenhouse Gas Control 16, 167-179.

595   Mason, H.E., Frane, W.L.D., Walsh, S.D.C., Dai, Z., Charnvanichborikarn, S., Carroll,

596   S.A., 2013. Chemical and mechanical properties of wellbore cement altered by CO_2-rich

597   brine using a multi analytical approach. Environ. Sci. Technol. 47, 1745−1752.

598 Nakano, K., Mito, S. and Xue, Z., 2017. Self-sealing of wellbore cement under the CO_2

599 batch experiment using well composite sample. Energy Procedia 114, 5212-5218.

600 Newell, D.L., Carey, J.W., 2013. Environ. Sci. Technol. 47, 276−282.

601 Onishi, T., Nguyen, M.C., Carey, J.W., Will, B., Zaluski, W., Bowen, D.W., Devault,

602 B.C., Duguid, A., Zhou, Q., Fairweather, S.H., Spangler, L.H., Stauffer, P.H., 2019.

603 Potential CO_2 and brine leakage through wellbore pathways for geologic CO_2

604 sequestration using the National Risk Assessment Partnership tools: Application to the

605 Big Sky Regional Partnership. Int. J. Greenh. Gas Cont. 81, 44−65.

606 Pang, X., 2015. The effect of water-to-cement ratio on the hydration kinetics of Portland

607 cement at different temperatures. In: The 14th international congress on cement

608 chemistry. Beijing, China; 2015.

609 Steefel C. I., Appelo C. A. J., Arora B., Jacques D., Kalbacher T., Kolditz O., Lagneau

610 V., Lichtner P. C., Mayer K. U., Meeussen J. C. L., Molins S., Moulton D., Shao H.,

611 Simunek J., Spycher N., Yabusaki S. B., Yeh G. T., 2015. Reactive transport codes for

612 subsurface environmental simulation. Computational Geosciences 19, 445-478.

613 Sterpenich, J., Jobard, E., El Hajj, H., Pironon, J., Randi, A. and Caumon, M.-C., 2014.

614 Experimental study of CO2 injection in a simulated injection well: the MIRAGES

615 experiment. Greenh. Gas.: Science and Technology 4, 210-224.Van Loon, L. R.,

616 Muller, W., Iijima, K., 2005. Activation energies of the self-diffusion of HTO, $^{22}Na^+$

617 and $^{36}Cl^-$ in a highly compacted argillaceous rock (Opalinus Clay). Appl. Geochem. 20,

618 961-972.

619 Walsh, S. D. C., Mason, H. E., Du Frane, W. L., Carroll, S. A., 2014. Experimental

620 calibration of a numerical model describing the alteration of cement/caprock interfaces

621 by carbonated brine. Int. J. Greenh. Gas Cont. 22, 176-188.

622 Wolery, T.J., Jackson, K.J., Bourcier, W.L., Bruton, C.J., Viani, B.E., Knauss,

623 K.G.,Delany, J.M., 1990. Current status of the EQ3/6 software package for geochemical

624 modeling. In: Melchior, C., Bassett, R.L. (Eds.), Chemical Modeling of Aqueous

625 Systems II. Am. Chem. Soc. Symp. Ser, vol. 416, pp. 104-116.

626 Zhang, M., Bachu, S., 2011. Review of integrity of existing wells in relation to CO_2

627 geological storage: What do we know? Int. J. Greenh. Gas Cont. 5, 826−840.

628 Zhang, L., Dzombak, D. A., Kutchko, B. G., 2015. Wellbore Cement Integrity under

629 Geologic Carbon Storage Conditions. Novel Materials for Carbon Dioxide Mitigation

630 Technology, 333–362.

631

Declaration of interests

☒ The authors declare that they have no known competing financial interests or personal relationships that could have appeared to influence the work reported in this paper.

☐The authors declare the following financial interests/personal relationships which may be considered as potential competing interests:

Author contributions

Lídia Fernández-Rojo: Investigation; Methodology; original draft; Writing - review & editing

Josep M. Soler: Validation; Writing - review & editing; Funding acquisition

M.Gabriela Dávila: Investigation; Methodology; Writing - review & editing

Carme Chaparro: Investigation; Methodology; Writing - review & editing

Ignasi Queralt: Methodology; Writing - review & editing

Jordi Cama: supervision; Writing - review & editing; Funding acquisition

FIGURE 1

FIGURE 2

A Inlet
supc-CO₂
Rock
Cement
47-49 mm
25 mm

Inlet
atm-CO₂
PVC films
Rock
Cement
24 mm
25 mm

B Inlet
Rock
Cement
Geometrical transformation

C Inlet
Zone 0
y
x
Rock
Cement
Zone 1
Zone 2
2D Model
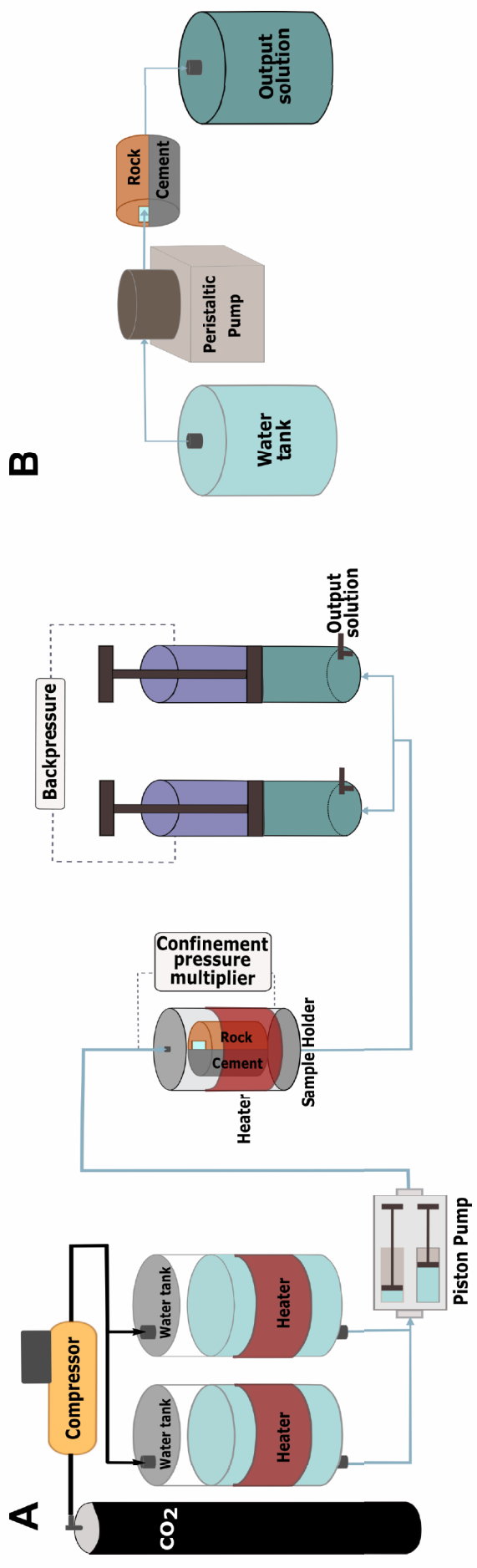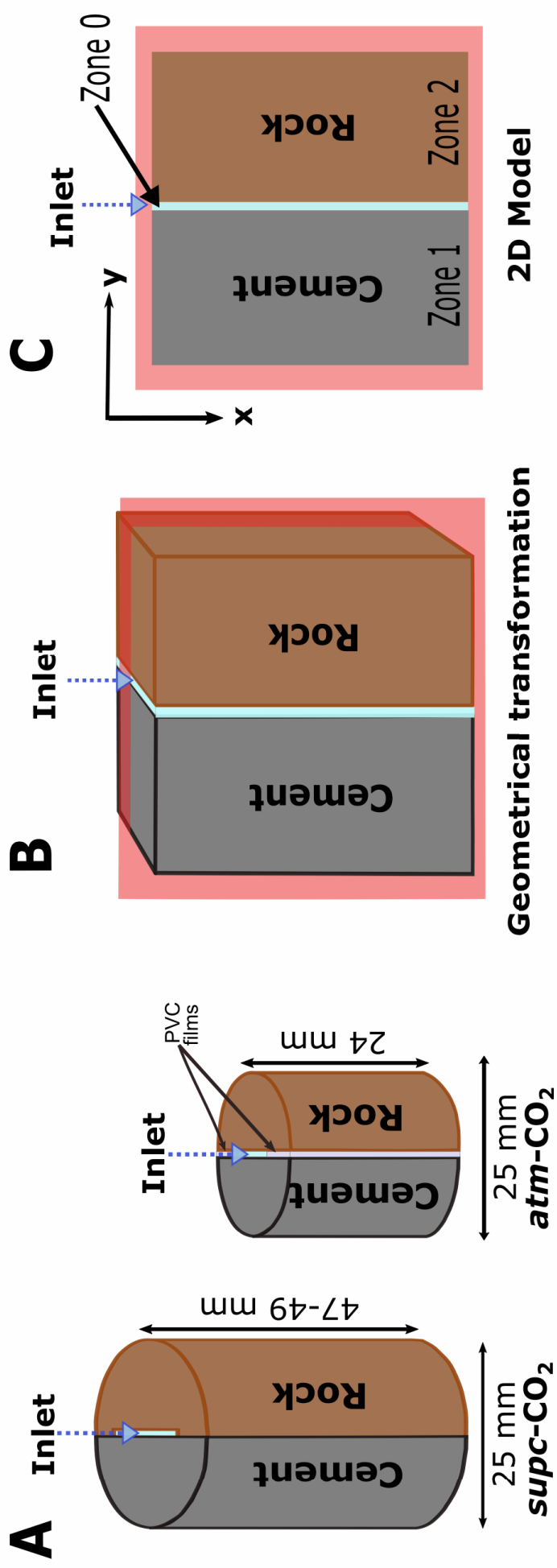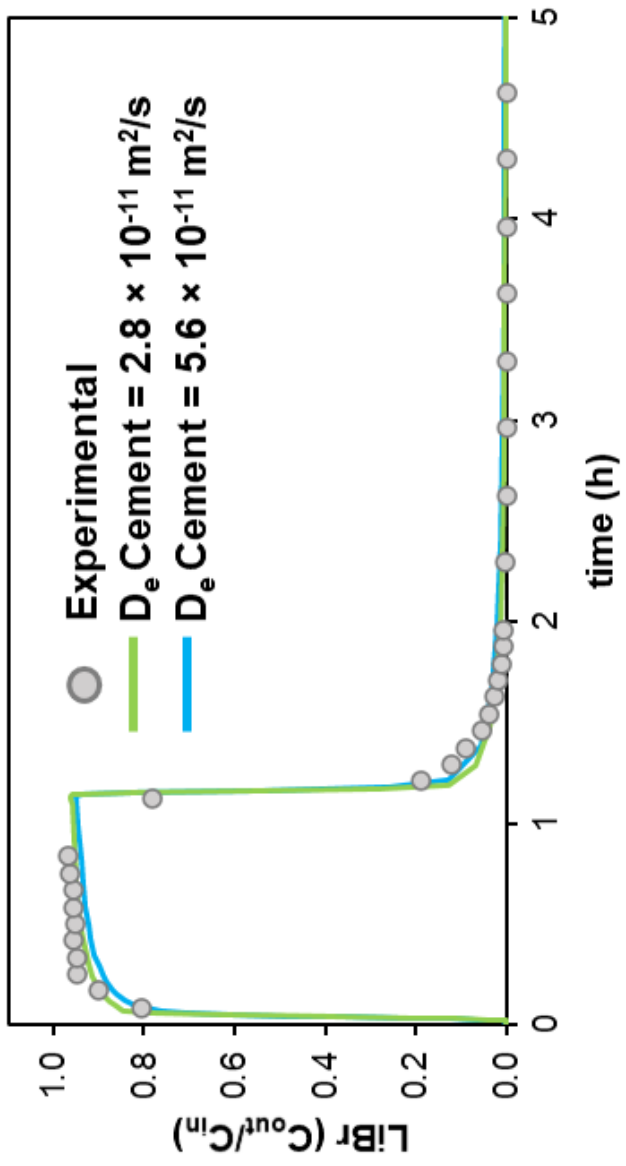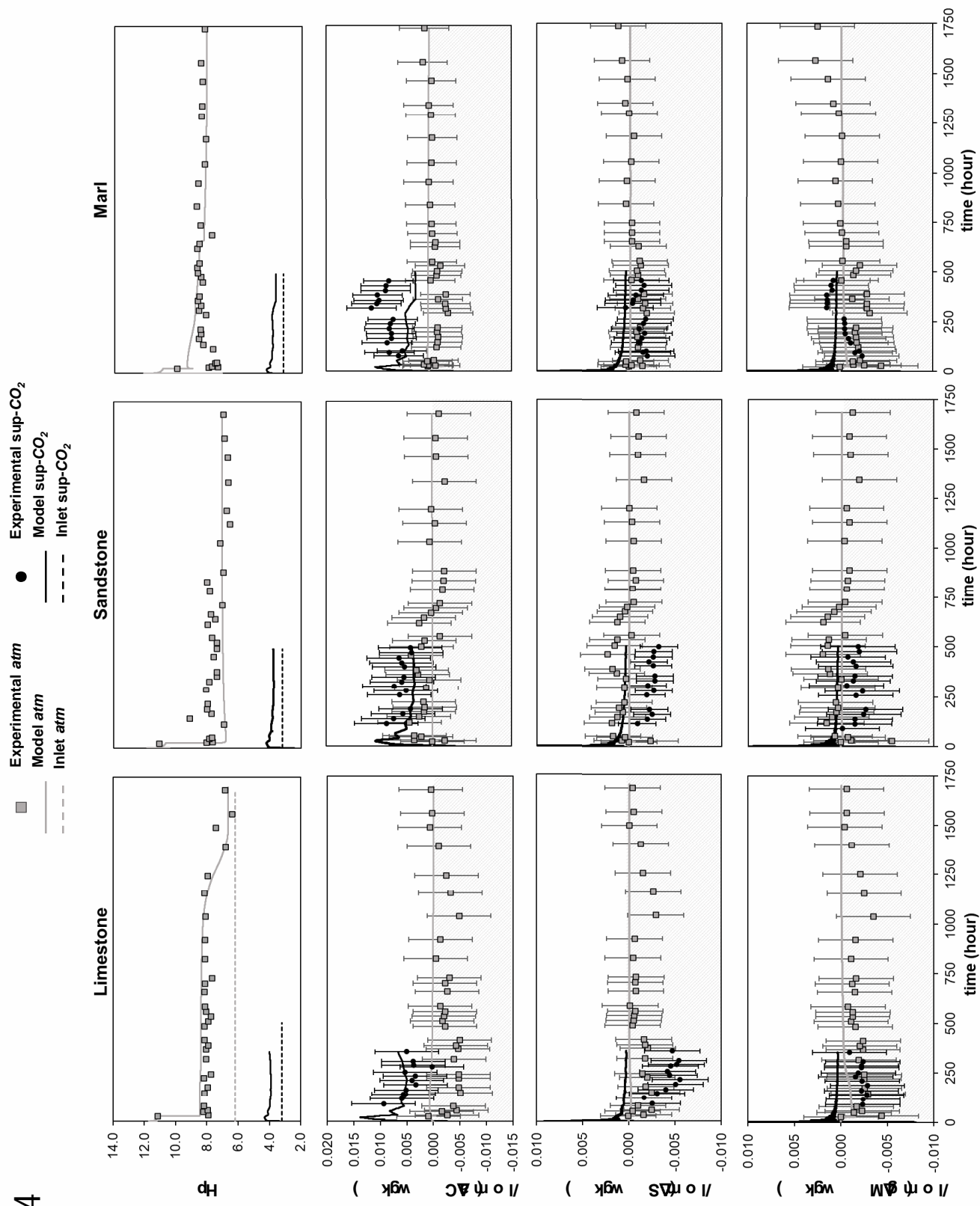
FIGURE 3

FIGURE 4

FIGURE 5

a) cement
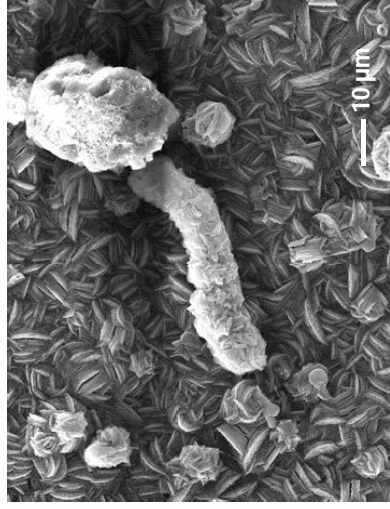
b) limestone
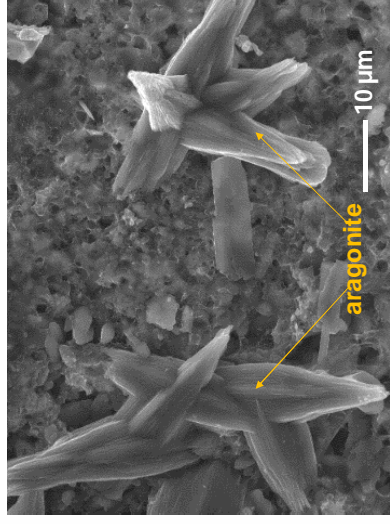
aragonite

10 µm

10 µm

c) sandstone

pristine zone | channel zone - reacted

channel limit

dissolved calcite

100 µm

d) marl

10 µm

FIGURE 6

a) cement

Fe nodule

50 µm

b) limestone

dissolved calcite

200 µm

c) sandstone

dissolved calcite

unaltered quartz

300 µm

d) marl

300 µm

FIGURE 7

	supc-LC	supc-SC	supc-MC	cement
measurement (mm³)	60	30	220	< 120
model (mm³)	77	36	103	482
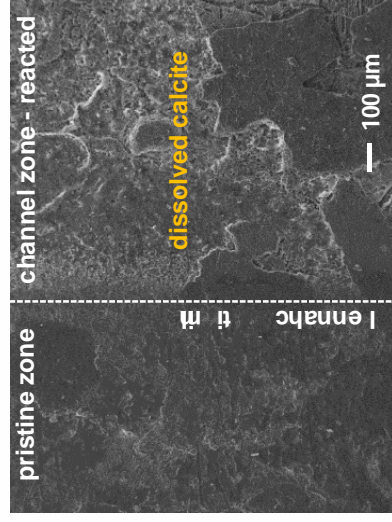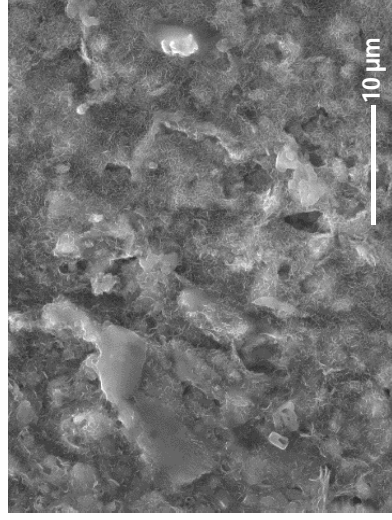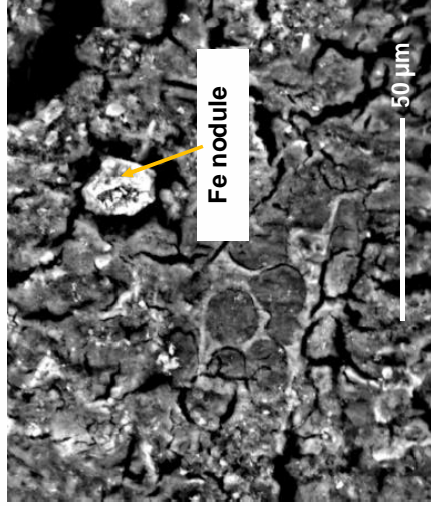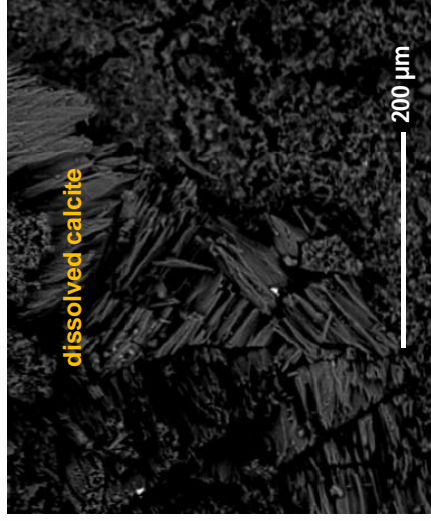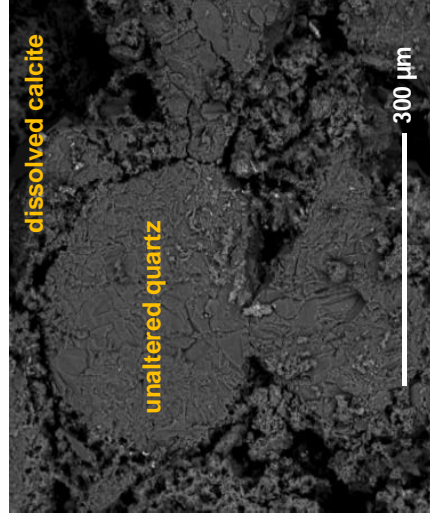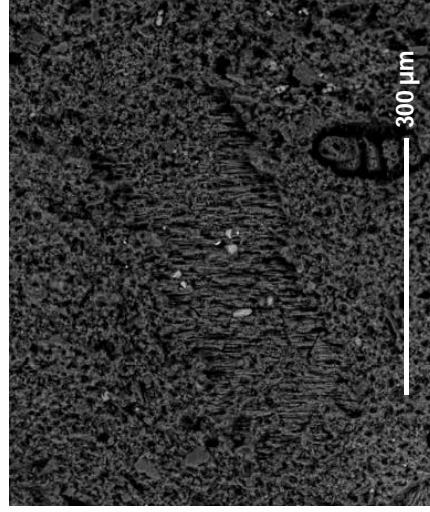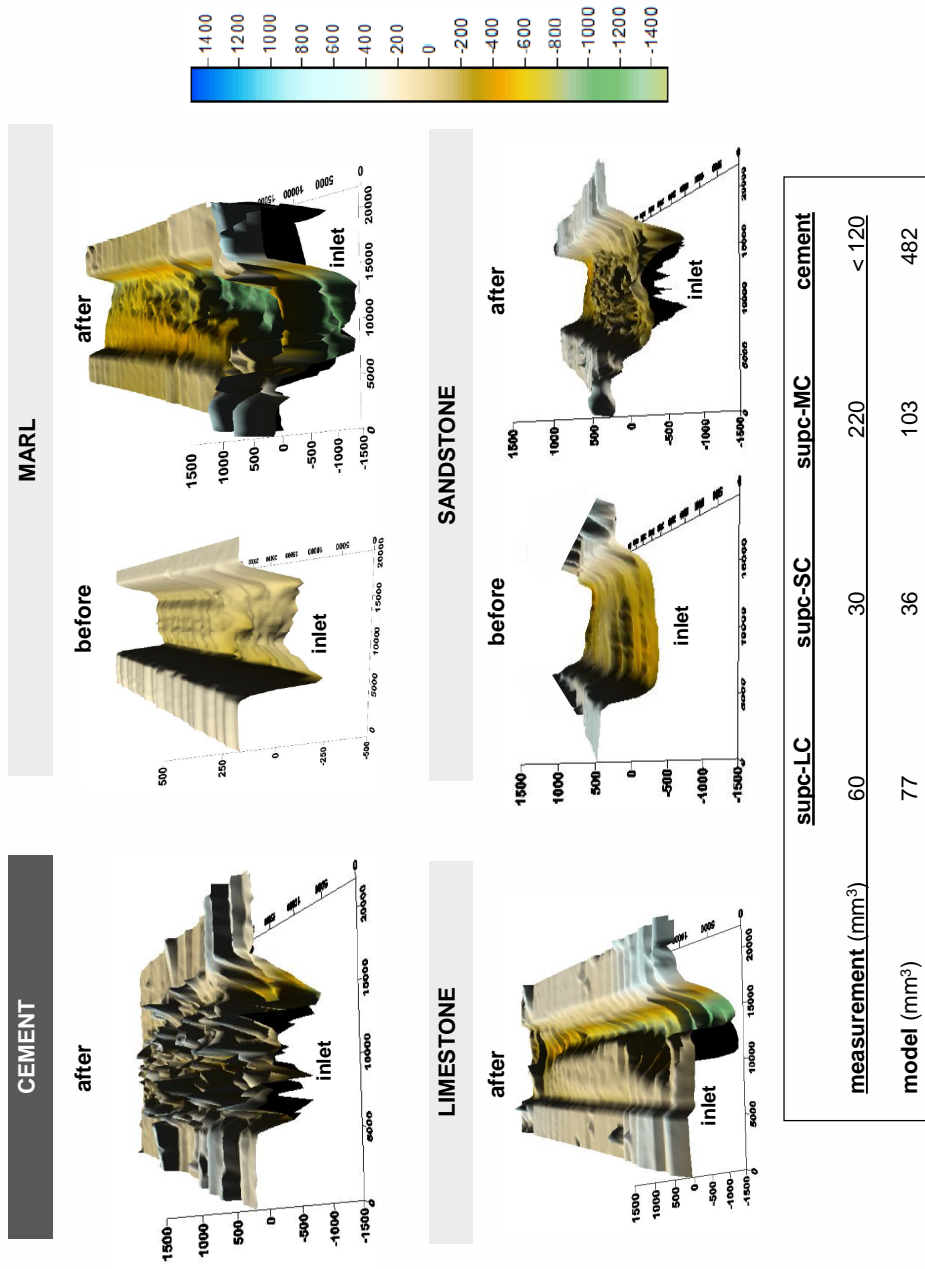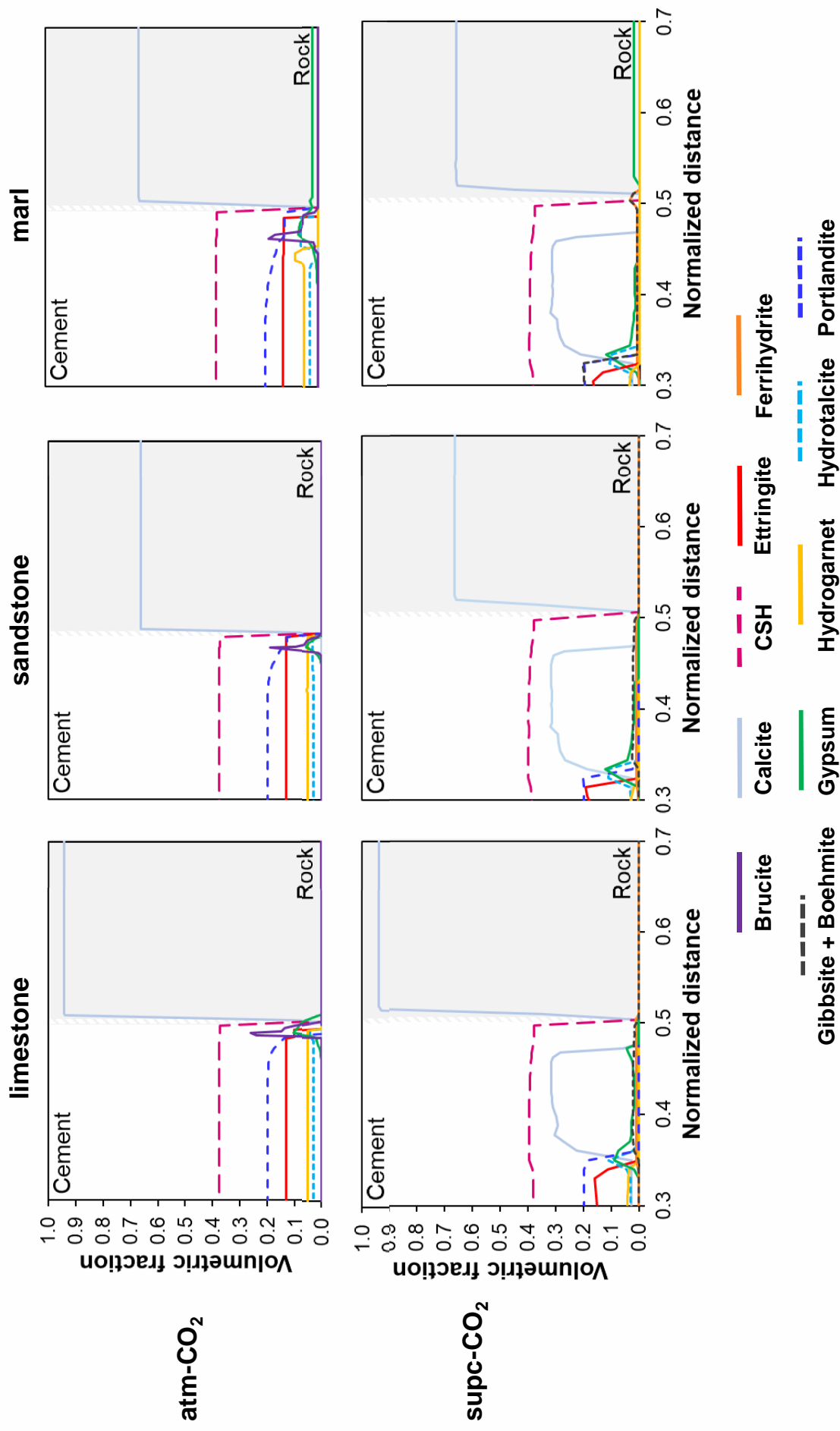
FIGURE 8

FIGURE 9
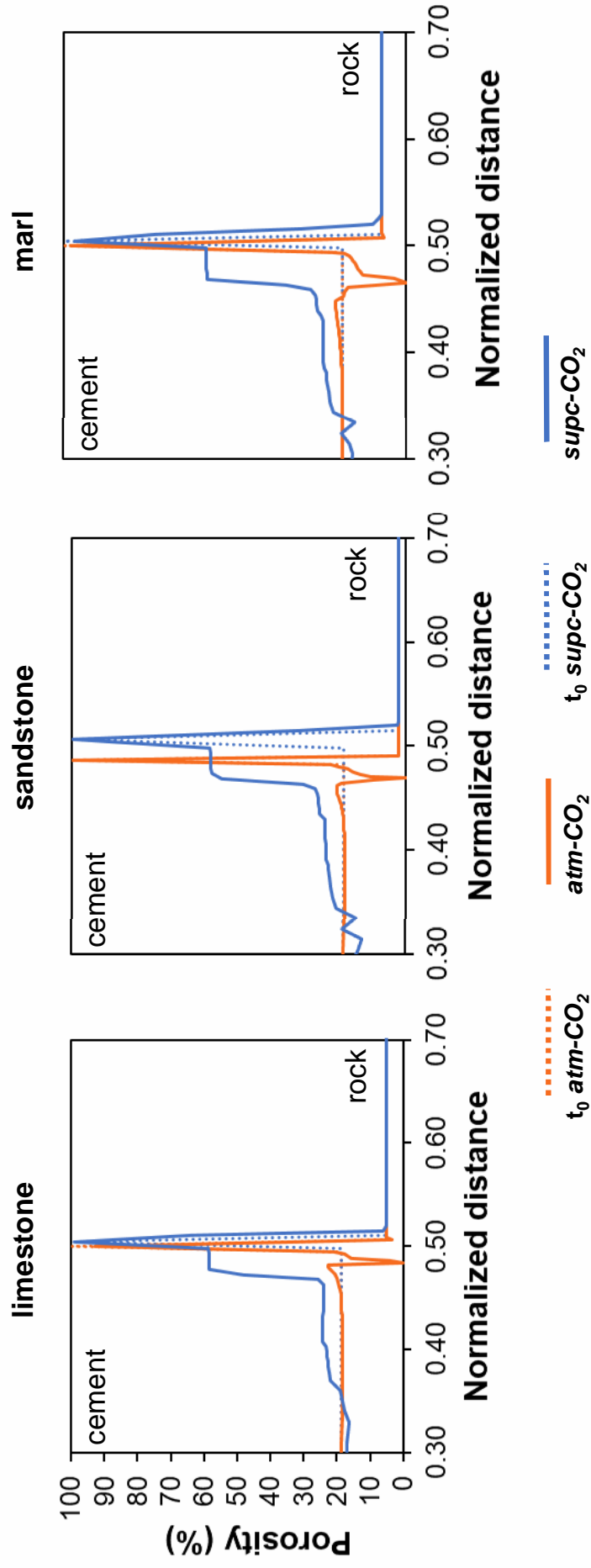
Table

Table 1 Experimental conditions.

experiment	rock	P_{CO_2} (bar)	T (ºC)	flow rate (mL/min)	experimental time (h)	residence time (s)	initial channel aperture (mm)	channel width (mm)	channel length (mm)	initial channel volume (mm^3)
supc-LC	limestone	130	60	0.06 ± 0.03	355	190	0.30*	13	47	176*
supc-SC	sandstone	130	60	0.06 ± 0.01	501	281	0.49*	12	48	272*
supc-MC	marl	130	60	0.06 ± 0.01	502	115	0.32*	12	49	121*
atm-LC	limestone	$10^{-3.4}$	25	0.05 ± 0.01	1683	160	0.50	10	24	120
atm-SC	sandstone	$10^{-3.4}$	25	0.05 ± 0.01	1685	160	0.50	10	24	120
atm-MC	marl	$10^{-3.4}$	25	0.049 ± 0.001	1735	147	0.50	10	24	120

*measured with confocal microscopy or profilometer

Permeability (k) of the rocks $< 10^{-18}$ m^2 (Dávila et al., 2016b)

Table 2. Chemical composition (total solute concentration in mol/kgw), ionic strength (I), and pH of the injected and initial porewater solutions used in the simulations. For the atm-CO$_2$ experiments it corresponds to the injected and porewater solutions after the initial tracer-test phase. See Table S3 for the chemical composition of the solutions used in the simulations of the tracer tests.

	supc-LC	*supc*-SC	*supc*-MC	*atm*-LC	*atm*-SC	*atm*-MC	Constraints
INPUT/CHANNEL							
Al^{3+}	1.00×10^{-6}	1.00×10^{-6}	1.00×10^{-6}	1.00×10^{-6}	1.00×10^{-6}	1.00×10^{-6}	known
Br$^-$	1.14×10^{-2}	1.14×10^{-2}	1.14×10^{-2}	1.14×10^{-2}	1.14×10^{-2}	1.14×10^{-2}	known
Ca^{2+}	4.73×10^{-2}	4.47×10^{-2}	4.25×10^{-2}	5.13×10^{-2}	4.71×10^{-2}	4.82×10^{-2}	known
Cl$^-$	4.89×10^{-1}	5.11×10^{-1}	4.83×10^{-1}	5.16×10^{-1}	4.89×10^{-1}	4.96×10^{-1}	known
CO$_{2(aq)}$	1.13	1.13	1.13	4.62×10^{-5}	3.11×10^{-5}	3.31×10^{-5}	calculated using Duan and Sun (2003) model (*supc*-CO$_2$) / equilibrium with CO$_2$(g) (*atm*-CO$_2$)
Fe^{2+}	1.50×10^{-4}	1.50×10^{-4}	1.50×10^{-4}	1.00×10^{-6}	1.00×10^{-6}	1.00×10^{-6}	known
K$^+$	1.14×10^{-2}	1.12×10^{-2}	1.09×10^{-2}	1.17×10^{-2}	1.13×10^{-2}	1.14×10^{-2}	known
Mg^{2+}	3.09×10^{-2}	3.15×10^{-2}	2.88×10^{-2}	3.31×10^{-2}	3.14×10^{-2}	3.14×10^{-2}	known
Na$^+$	3.86×10^{-1}	4.02×10^{-1}	3.82×10^{-1}	4.03×10^{-1}	3.84×10^{-1}	3.90×10^{-1}	known
O$_{2(aq)}$	1.61×10^{-4}	1.61×10^{-4}	1.61×10^{-4}	2.84×10^{-4}	2.84×10^{-4}	2.84×10^{-4}	known
SiO$_{2(aq)}$	1.00×10^{-6}	1.00×10^{-6}	1.00×10^{-6}	1.00×10^{-6}	1.00×10^{-6}	1.00×10^{-6}	known
SO$_4^{2-}$	2.67×10^{-2}	2.13×10^{-2}	2.09×10^{-2}	2.76×10^{-2}	2.59×10^{-2}	2.66×10^{-2}	known
I	0.59	0.60	0.57	0.63	0.60	0.61	-
pH	3.21	3.26	3.13	6.41	6.17	6.21	charge balance (*supc*-CO$_2$)/known (*atm*-CO$_2$)
CEMENT							
Al^{3+}	1.03×10^{-4}	1.03×10^{-4}	1.03×10^{-4}	8.97×10^{-5}	8.97×10^{-5}	8.97×10^{-5}	hydrogarnet
Br$^-$	1.00×10^{-9}	1.00×10^{-9}	1.00×10^{-9}	1.00×10^{-9}	1.00×10^{-9}	1.00×10^{-9}	fixed
Ca^{2+}	6.10×10^{-4}	6.10×10^{-4}	6.10×10^{-4}	1.01×10^{-3}	1.01×10^{-3}	1.01×10^{-3}	portlandite
Cl$^-$	1.00×10^{-9}	1.00×10^{-9}	1.00×10^{-9}	1.00×10^{-9}	1.00×10^{-9}	1.00×10^{-9}	fixed
CO$_{2(aq)}$	7.70×10^{-5}	7.70×10^{-5}	7.70×10^{-5}	1.23×10^{-4}	1.23×10^{-4}	1.23×10^{-4}	calcite

	supc-LC	supc-SC	supc-MC	atm-LC	atm-SC	atm-MC	Constraints
Fe^{2+}	6.91×10^{-8}	6.91×10^{-8}	6.91×10^{-8}	6.91×10^{-8}	6.91×10^{-8}	6.91×10^{-8}	Known
K^+	3.44×10^{-1}	3.44×10^{-1}	3.44×10^{-1}	3.44×10^{-1}	3.44×10^{-1}	3.44×10^{-1}	known
Mg^{2+}	4.74×10^{-9}	4.74×10^{-9}	4.74×10^{-9}	5.57×10^{-10}	5.57×10^{-10}	5.57×10^{-10}	hydrotalcite
Na^+	1.28×10^{-2}	1.28×10^{-2}	1.28×10^{-2}	1.28×10^{-2}	1.28×10^{-2}	1.28×10^{-2}	known
$O_{2(aq)}$	1.61×10^{-4}	1.61×10^{-4}	1.61×10^{-4}	2.84×10^{-4}	2.84×10^{-4}	2.84×10^{-4}	fixed
$SiO_{2(aq)}$	8.65×10^{-6}	8.65×10^{-6}	8.65×10^{-6}	3.45×10^{-5}	3.45×10^{-5}	3.45×10^{-5}	CSH
SO_4^{2-}	6.90×10^{-2}	6.90×10^{-2}	6.90×10^{-2}	2.34×10^{-3}	2.34×10^{-3}	2.34×10^{-3}	ettringite
I	0.38	0.38	0.38	0.34	0.34	0.34	-
pH	12.19	12.19	12.19	13.35	13.35	13.35	charge balance
ROCK							
Al^{3+}	1.00×10^{-9}	1.00×10^{-9}	1.00×10^{-9}	1.00×10^{-9}	1.00×10^{-9}	1.00×10^{-9}	fixed
Br^-	1.14×10^{-2}	1.14×10^{-2}	1.14×10^{-2}	1.14×10^{-2}	1.14×10^{-2}	1.14×10^{-2}	fixed
Ca^{2+}	4.74×10^{-2}	4.45×10^{-2}	4.27×10^{-2}	5.13×10^{-2}	4.73×10^{-2}	3.76×10^{-2}	calcite
Cl^-	4.89×10^{-1}	5.11×10^{-1}	4.83×10^{-1}	5.16×10^{-1}	4.89×10^{-1}	4.89×10^{-1}	fixed
$CO_{2(aq)}$	1.92×10^{-4}	1.97×10^{-4}	1.97×10^{-4}	4.38×10^{-4}	4.46×10^{-4}	4.46×10^{-4}	equilibrium with $CO_{2(g)}$
Fe^{2+}	1.00×10^{-11}	1.00×10^{-11}	1.00×10^{-11}	1.00×10^{-9}	1.00×10^{-9}	1.00×10^{-9}	fixed
K^+	1.14×10^{-2}	1.12×10^{-2}	1.14×10^{-2}	1.17×10^{-2}	1.13×10^{-2}	1.17×10^{-2}	fixed
Mg^{2+}	3.09×10^{-2}	3.15×10^{-2}	2.88×10^{-2}	3.31×10^{-2}	3.14×10^{-2}	3.31×10^{-2}	fixed
Na^+	3.86×10^{-1}	4.02×10^{-1}	3.82×10^{-1}	4.03×10^{-1}	3.84×10^{-1}	3.84×10^{-1}	fixed
$O_{2(aq)}$	1.61×10^{-4}	1.61×10^{-4}	1.61×10^{-4}	2.84×10^{-4}	2.84×10^{-4}	2.84×10^{-4}	fixed
$SiO_{2(aq)}$	3.17×10^{-4}	3.18×10^{-4}	3.19×10^{-4}	8.93×10^{-5}	9.00×10^{-5}	9.08×10^{-5}	quartz
SO_4^{2-}	2.67×10^{-2}	2.13×10^{-2}	2.09×10^{-2}	2.76×10^{-2}	2.59×10^{-2}	2.66×10^{-2}	fixed
I	0.59	0.60	0.57	0.63	0.60	0.56	-
pH	7.39	7.40	7.41	7.50	7.51	7.56	charge balance

Table 3. Adjusted mineral bulk surface areas (BSA in $m^2_{mineral}/m^3_{porous\ medium}$) of primary and secondary phases used in the simulations. For primary phases, initial vol.% is indicated in parenthesis. Shaded values are values reduced to obtain a good match between model and experimental results.

	supc-LC	supc-SC	supc-MC	atm-LC	atm-SC	atm-MC
CHANNEL (Zone 0)						
Secondary minerals BSA						
Albite	NA	NA	1.0×10^5	NA	NA	1.0×10^5
Aragonite	NA	NA	NA	1.0×10^5	1.0×10^5	1.0×10^5
Boehmite	1.0×10^5	1.0×10^5	1.0×10^5	NA	NA	NA
Brucite	NA	NA	NA	1.0×10^{-5}	5.0×10^1	1.0×10^{-5}
Calcite	1.0×10^5	1.0×10^5	1.0×10^5	NA	NA	NA
Calcite-dissolution only	NA	NA	NA	1.0×10^5	1.0×10^5	1.0×10^5
Clinochlore	NA	NA	NA	NA	NA	1.0×10^5
CSH	1.0×10^5	1.0×10^5	1.0×10^5	1.0×10^5	1.0×10^5	1.0×10^5
Dolomite	1.0×10^5	1.0×10^5	1.0×10^5	NA	NA	NA
Ettringite	1.0×10^5	1.0×10^5	1.0×10^5	8.0×10^2	1.0×10^1	1.0×10^2
Ferrihydrite	1.0	1.0×10^1	1.0	NA	NA	NA
Gibbsite	1.0×10^5	1.0×10^5	1.0×10^5	NA	NA	NA
Gypsum	1.0	1.0	1.0	1.0	1.0	1.0
Hydrogarnet	1.0×10^5	1.0×10^5	1.0×10^5	1.0×10^2	1.0×10^2	1.0×10^5
Hydrotalcite	1.0×10^5	1.0×10^5	1.0×10^5	1.0×10^5	1.0×10^5	1.0×10^5
Illite	NA	NA	1.0×10^5	NA	NA	1.0×10^5
Kaolinite	1.0×10^5	1.0×10^5	1.0×10^5	NA	NA	NA
Microcline	NA	1.0×10^5	NA	NA	1.0×10^5	NA
Monosulfate	1.0×10^5	1.0×10^5	1.0×10^5	1.0×10^5	1.0×10^5	1.0×10^5
Portlandite	1.0×10^5	1.0×10^5	1.0×10^5	8.0×10^2	1.0×10^1	1.0×10^2
Pyrite	NA	NA	1.0×10^5	NA	NA	1.0×10^5
Quartz	1.0×10^5	1.0×10^5	1.0×10^5	1.0×10^5	1.0×10^5	1.0×10^5
CEMENT (Zone 1)						
Primary minerals BSA (Vol. F %)						
Calcite	1.0×10^5 (2.73)	1.0×10^5 (2.73)	1.0×10^5 (2.73)	NA	NA	NA
Calcite-dissolution only	NA	NA	NA	1.0×10^5 (2.73)	1.0×10^5 (2.73)	1.0×10^5 (2.73)

	supc-LC	supc-SC	supc-MC	atm-LC	atm-SC	atm-MC
CSH-1667	1.0×10^5 (37.68)	1.0×10^5 (37.68)	1.0×10^5 (37.68)	1.0×10^5 (37.68)	1.0×10^5 (37.68)	1.0×10^5 (37.68)
Ettringite	1.0×10^5 (13.31)	1.0×10^5 (13.31)	1.0×10^5 (13.31)	8.0×10^2 (13.31)	1.0×10^1 (13.31)	1.0×10^2 (13.31)
Hydrogarnet	1.0×10^5 (4.97)	1.0×10^5 (4.97)	1.0×10^5 (4.97)	1.0×10^2 (4.97)	1.0×10^2 (4.97)	1.0×10^5 (4.97)
Hydrotalcite	1.0×10^5 (2.95)	1.0×10^5 (2.95)	1.0×10^5 (2.95)	1.0×10^5 (2.95)	1.0×10^5 (2.95)	1.0×10^5 (2.95)
Portlandite	1.0×10^5 (19.76)	1.0×10^5 (19.76)	1.0×10^5 (19.76)	8.0×10^2 (19.76)	1.0×10^1 (19.76)	1.0×10^2 (19.76)

Secondary minerals
BSA

	supc-LC	supc-SC	supc-MC	atm-LC	atm-SC	atm-MC
Aragonite	NA	NA	NA	1.0×10^5	1.0×10^5	1.0×10^5
Boehmite	1.0×10^5	1.0×10^5	1.0×10^5	NA	NA	NA
Brucite	NA	NA	NA	1.0×10^{-5}	5.0×10^1	1.0×10^{-5}
Dolomite	1.0×10^5	1.0×10^5	1.0×10^5	NA	NA	NA
Ferrihydrite	1.0	1.0×10^1	1.0	NA	NA	NA
Gibbsite	1.0×10^5	1.0×10^5	1.0×10^5	NA	NA	NA
Gypsum	1.0	1.0	1.0	1.0	1.0	1.0
Kaolinite	1.0×10^5	1.0×10^5	1.0×10^5	NA	NA	NA
Monosulfate	1.0×10^5	1.0×10^5	1.0×10^5	1.0×10^5	1.0×10^5	1.0×10^5

ROCK (Zone 2)
Primary minerals BSA (Vol. F %)

	supc-LC	supc-SC	supc-MC	atm-LC	atm-SC	atm-MC
Albite	NA	NA	1.0×10^5 (6.28)	NA	NA	1.0×10^5 (6.28)
Calcite	1.0×10^5 (94.04)	1.0×10^5 (66.24)	1.0×10^5 (66.02)	1.0×10^5 (94.04)	1.0×10^5 (66.24)	1.0×10^5 (66.02)
Chlinochlore	NA	NA	1.0×10^5 (2.66)	NA	NA	1.0×10^5 (2.66)
Gypsum	NA	NA	1.0×10^5 (2.13)	NA	NA	1.0×10^5 (2.13)
Illite	NA	1.0×10^5 (4.53)	1.0×10^5 (6.44)	NA	1.0×10^5 (4.53)	1.0×10^5 (6.44)
Microcline	NA	1.0×10^5 (2.29)	NA	NA	1.0×10^5 (2.29)	NA
Pyrite	NA	NA	1.0×10^5 (0.10)	NA	NA	1.0×10^5 (0.10)
Quartz	1.0×10^5 (0.42)	1.0×10^5 (23.89)	1.0×10^5 (9.20)	1.0×10^5 (0.42)	1.0×10^5 (23.89)	1.0×10^5 (9.20)

Secondary minerals
BSA

	supc-LC	supc-SC	supc-MC	atm-LC	atm-SC	atm-MC
Gypsum	1.0×10^5	1.0×10^5	NA	1.0×10^5	1.0×10^5	NA
Ferrihydrite	1.0×10^5	1.0×10^5	1.0×10^5	NA	NA	NA

	supc-LC	supc-SC	supc-MC	atm-LC	atm-SC	atm-MC
Kaolinite	1.0×10^5	1.0×10^5	1.0×10^5	NA	NA	NA

NA: the mineral has not been considered in the simulation.

Shaded values indicate reduced values.

Table 4. Transport parameters used in the simulations.

	supc-LC	supc-SC	supc-MC	atm-LC	atm-SC	atm-MC
Darcy velocity (m^3/m^2/s)	2.47×10^{-4}	1.65×10^{-4}	2.75×10^{-4}	1.53×10^{-4}	1.50×10^{-4}	1.63×10^{-4}
Longitudinal dispersivity (m)	0.001	0.001	0.001	0.001	0.001	0.001
CHANNEL (Zone 0)						
D_{eff} (m^2/s)	1.0×10^{-9}	1.0×10^{-9}	1.0×10^{-9}	1.0×10^{-9}	1.0×10^{-9}	1.0×10^{-9}
Porosity (Vol. F %)	100	100	100	100	100	100
CEMENT (Zone 1)				-	-	
D_{eff} (m^2/s)	6.5×10^{-11}	6.5×10^{-11}	6.5×10^{-11}	5.6×10^{-11}	2.8×10^{-11}	5.6×10^{-11}
Porosity (Vol. F %)	18.60	18.60	18.60	18.60	18.60	18.60
ROCK (Zone 2)						
D_{eff} (m^2/s)	2.5×10^{-12}	1.03×10^{-12}	3.59×10^{-12}	5.0×10^{-13}	2.1×10^{-13}	7.2×10^{-13}
Porosity (Vol. F %)	5.00	2.05	7.27	5.00	2.05	7.27

D_{eff} = effective diffusion coefficient